Microporous and Mesoporous Materials 377 (2024) 113202

Contents lists available at ScienceDirect

Microporous and Mesoporous Materials

journal homepage: www.elsevier.com/locate/micromeso

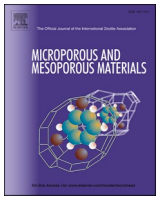

MRI and PFG NMR studies of percolation effects in advanced melting during a cryoporometry characterisation of disordered mesoporous alumina

Eleni Himona [a], Lee Stevens [a], Huw Williams [b], Sean P. Rigby [a,*]

[a] Department of Chemical and Environmental Engineering, Faculty of Engineering, University of Nottingham, University Park, Nottingham, NG7 2RD, UK
[b] Centre for Biomolecular Sciences, University of Nottingham, University Park, Nottingham, NG7 2RD, UK

ARTICLE INFO

Keywords:
NMR cryoporometry
MRI
Alumina
Pore network
Advanced melting

ABSTRACT

Cryoporometry (or thermoporometry) offers a way of pore structural characterisation for mesoporous materials that often needs little sample preparation, is relatively quick, and is statistically-representative for macroscopic samples. While it is well-known that freezing is controlled by pore-blocking, and is thus an invasion percolation process, the percolative nature of pore-to-pore co-operative advanced melting effects has been much less studied. In this work, PFG NMR studies, of diffusivity within the molten phase, have shown that the early melting process follows the scaling law, expected from percolation theory, below the percolation threshold. The percolation threshold thereby obtained was that for a 3D isotropic Poisson polyhedral lattice, consistent with the observation of patchwise macroscopic heterogeneities in the spatial distribution of local average pore size seen in MR relaxation time-weighted images. MRI has shown that once advanced melting effects kicked-in, around the percolation threshold, they occurred to different degrees in different slices along the length of the extrudate pellet. The macroscopic banding in pore-blocking, during freezing, and advanced melting effects, along the axis of the extrudate was consistent with anisotropic diffusional properties observed with MRI. Hence, it has been shown how the pore-pore co-operative effects can be utilised to improve structural characterisation of mesoporous solids.

1. Introduction

Given the abundant applications of amorphous, nanoporous materials in catalysis, batteries, fuel cells, gas separations, controlled drug delivery etc., methods are required to characterise the porous structure in order for quality control in synthesis, and for obtaining fundamental understanding of the relevant physico-chemical processes that take place within the void space during these applications. Indirect methods of pore characterisation still have significant advantages over more direct imaging methods, such as more representative sampling of heterogeneous materials, and the ability to detect pore sizes over wider ranges in just one, often much quicker, experiment. Cryoporometry, also known as thermoporometry, is an indirect technique with many additional advantages. In particular, it can look at wet samples, using the liquid already present as the probe fluid. This means it can be used to study materials part-way through fabrication processes, such as at the precipitation stage for inorganic solids. It can also be used to study systems that evolve following immersion, such as controlled drug delivery systems [1,2].

Cryoporometry is based upon the principle that the melting and freezing points of fluids in confined geometries are depressed below the bulk value by an amount inversely proportional to the characteristic dimension of the pore. The resulting relation between the, say, melting point depression ΔT_m and the characteristic pore size d is typically referred to as the Gibbs-Thomson equation [3]:

$$\Delta T_m = \frac{k}{(d - 2t)}, \tag{1}$$

where k is a constant of proportionality that depends upon the properties of the probe fluid, and t is the thickness of the non-freezing layer that arises at the solid surface for most systems [4]. The simplest experiment consists of completely freezing the probe fluid within the pores of the sample, and then progressively raising the temperature in small discrete steps, or as a slow ramp, and measuring the amount of probe fluid

* Corresponding author.
E-mail address: sean.rigby@nottingham.ac.uk (S.P. Rigby).

https://doi.org/10.1016/j.micromeso.2024.113202
Received 27 March 2024; Received in revised form 14 May 2024; Accepted 3 June 2024
Available online 4 June 2024

melting at each temperature. Eq. (1) is then used to relate the melting temperature to the pore size, while the amount of probe melting delivers the pore volume. The amount of probe fluid melting can be monitored either using the heat-flow arising from the latent heat of fusion via differential scanning calorimetry (DSC), or using NMR with a relaxation time filter to distinguish solid from liquid [5].

There is some debate about the correct value of k to use, even for the same fluid in the same type of solid. For example, Gun'ko et al. [6] suggested k for melting of water (according to a cylindrical sleeve meniscus) in silica pores was 67 K nm, but does not report how this value was obtained. In contrast, Findenegg et al. [7] suggested k was 52 ± 2 K nm. From a survey of the relevant literature, Rottreau et al. [8] found that the range of k values previously obtained for water lies between 49 and 58 K nm. Much previous work on trying to calibrate k has used templated, controlled pore size materials, such as SBA-15 [7], but, more recently, attempts have been made to use dual-fluid thermoporometry to internally calibrate k for amorphous materials [9].

It is generally observed in cryoporometry experiments that the melting and freezing branches do not occur at the same temperature, and thus exhibit hysteresis. Petrov and Furó [3] considered that the freezing-melting hysteresis in cryoporometry arises due to a free energy barrier between metastable and stable states of the pore filling material. In a phenomenological description, these workers showed that freezing point depression is given by:

$$\Delta T_f \cong -\frac{\upsilon \gamma_{sl} T^0}{\Delta H} \frac{S}{V}, \tag{2}$$

while the melting point depression is given by:

$$\Delta T_m \cong -\frac{\upsilon \gamma_{sl} T^0}{\Delta H} \frac{\partial S}{\partial V}, \tag{3}$$

where υ is the molar volume, γ_{sl} is the surface free energy, T^0 is the bulk melting point, S is the surface area of the pore, V is the volume of the pore, and ΔH is the latent heat of melting. Utilising the formula for equidistant surfaces due to Steiner, Petrov and Furó [3] showed that eq. (3) can be rewritten as:

$$\Delta T_m \cong -\frac{\upsilon \gamma_{sl} T^0}{\Delta H} 2\kappa = \Delta T_f \frac{2\kappa V}{S} = \frac{K}{(d - 2t)} \tag{4}$$

where κ is the integral mean curvature of the pore surface. For a cylindrical pore of diameter d, then $2\kappa V/S = 1/2$, and, hence, the numerical difference in ΔT_m and ΔT_f can be used to determine whether a pore has an open cylindrical geometry. Implicit in eq. (4), is the conception that, upon freezing, liquid solidifies in an axial direction initiated from the end where the liquid is in contact with bulk solid, while melting commences at the liquid film at the pore surface and propagates radially from the surface toward the pore bulk. However, for a dead-end cylindrical pore, melting can occur axially, since it would then be initiated from the hemispherical meniscus at the closed end of the pore. Similarly melting can be initiated from a hemispherical meniscus located at the interface between frozen and molten phases within co-axial, adjoining cylindrical pores of differing diameters [5]. This will be discussed in more detail below.

In a disordered porous solid the phase transitions occurring during a cryoporometry experiment can be a complex function of the void space geometry and topology [5]. While a typical system will reach an equilibrium, in a quasi-static, stepwise temperature change melting experiment, where the interface between the molten and frozen pore cores remains stable over time, the particular position this front achieves, at a given temperature, depends upon the spatial disposition and connectivity of the various segments of the void space with different characteristic dimension d. This means that the distribution of characteristic sizes of the molten and frozen void space segments, at a given temperature on the melting curve, depends upon how these segments are connected up. The simplest interpretation assumes that the void space consists of a bundle of isolated, parallel-sided, straight cylindrical pores (a 'wine-rack' type structure).

Freezing can occur via two mechanisms, namely homogeneous nucleation and heterogeneous nucleation [3]. The former occurs when there is no residual ice present to act as a seed, and, thus, occurs only with supercooling to very low temperatures well below the equilibrium value, where the kinetic barrier to the phase change is eventually overcome. The latter will occur when, say, an ice wall of frozen bulk film, is left surrounding a porous pellet. Heterogeneous nucleation results in freezing occurring as an invasion percolation process. This is because, as is evident from consideration of a simple ink-bottle geometry, if the ice wall is present at the outer mouth of the pore neck, then freezing can only occur in the ink-bottle once the temperature has dropped low enough to commence freezing in the neck. Once the neck is frozen, freezing will be initiated in the pore body, as it will already be below the critical freezing temperature. This effect is similar to 'pore--blocking' or 'pore-shielding' seen in gas desorption and mercury intrusion [5].

Melting can also occur via two mechanisms. First, it can be nucleated by the non-freezing layer found at the boundary between the ice in the core of the pore and the solid wall. In that case, in a cylindrical geometry, melting occurs in a radial direction by growth of the surface molten film towards the centre of the pore. Once, one pore is fully molten, in cylindrical geometry, it presents a full hemispherical meniscus at the ends of the pore forming the boundary with the next pore. This can facilitate melting in an axial direction along the pore axis of the neighbouring pores. The melting temperature for axial melting is typically lower than that for radial melting in the same pore. Hence, in a connected network of pores, the melting of one pore, via radial melting (nucleation), can facilitate the melting of a neighbouring pore at a lower temperature than otherwise expected for isolated pores. In some cases the critical temperature for axial melting of a larger pore body is lower than the temperature for the radial melting of a neighbouring pore neck, and so the two void space elements can melt together at the same temperature. This process is known as advanced melting [10]. Even if this does not apply, the presence of a hemispherical meniscus adjoining a given pore will lower the critical temperature for melting. Together, these effects result in a cascade growth of the molten phase known as phase expansion [11,12], which is potentially an ordinary percolation process, and this will be investigated here.

However, the pore-to-pore co-operative melting only tends to work for ratios of pore body-to-pore neck sizes up to a critical cut-off value, that classical theory suggests is a factor of 2, though it may be higher for some probe fluids like water [10,13]. However, unlike freezing, where the invading ice phase advances from the sample periphery, advanced melting can be initiated throughout the network and proceed in any direction, rather than just mainly inwards like freezing. However, the idiosyncratic characteristics of pore-blocking and advanced melting mean that the pore-to-pore co-operative effects can be deconvolved to some extent, and, thus, used in pore network characterisation [5]. Advanced melting has been observed in a range of porous materials, including silicas [10] and cements [14]. Recently, a detailed one-dimensional corrugated pore model has been developed to study advanced melting phenomena, and has been found to reproduce, qualitatively, many of the forms of experimental data anticipated when advanced melting is active [11].

Enniful et al. [11] suggested that, as the temperature rises on melting, then the number of melting nucleation events can increase (as more pores are above the critical temperature for initiating radial melting), which diminishes the role of phase expansion, controlled by percolation. However, this general assertion only applies for large, well-connected, random systems, where nucleation sites will be pervasive and common, and joined to other sites. The balance between nucleation and phase expansion dominated melting will depend strongly on the nature of any spatial distribution and/or correlation of pore sizes.

The pore-to-pore co-operative nature of both pore-blocking and

advanced melting means they can, potentially, lead to phase transitions in a sample-spanning cascade [5]. This suggests the importance of spatially-resolved techniques for understanding such systems. Indeed, cryoporometry has been combined with magnetic resonance imaging (MRI) to obtain spatially-resolved pore size distributions, since the melting processes can be monitored for individual voxel volumes in the MR image [15]. Further, while advanced adsorption phenomena have been probed using spatially-resolved NMR relaxation time images to provide an independent measure of the pore sizes of condensed phase [13,16], the advanced melting process has not been studied via MRI. It is the purpose of this work to study advanced melting processes using MRI. In addition, while pulsed-field gradient (PFG) NMR has been used to probe the connectivity of adsorbed ganglia in partially saturated mesoporous solids [13], it has not been used to probe the potential percolative nature of the melting transition. This will also be the subject of this work.

The main aim of this study is to test for potential percolative behaviour in the advanced melting process using MRI to study spatial sample-spanning phenomena and PFG NMR to study the connectivity of the molten phase across the phase transition. Given the common presence of pore-blocking in all three techniques, the NMR cryoporometry data will be compared with corresponding findings from gas sorption scanning curves and mercury porosimetry. Scanning curves are proposed to implicitly contain all information about the network [11], and, as will be described below, the form can be used to assess the degree of disorder in the void space [5,11]. In this work we use gas sorption scanning curve data in a qualitative, type-classification to distinguish between relatively weak and strong disorder. This study consists of a case study of a material that has previously been shown to possess macroscopic heterogeneities in the spatial arrangement of porosity and pore size using MRI [17,18], since such a material is most likely to exhibit large length-scale correlations in behaviour that will be evident with MRI and PFG.

2. Theory

2.1. Percolation theory

Percolation theory provides a general framework for describing the mass transport properties of network structures in terms of lattice models [19]. In percolation theory, the dependence of any property of the pore space is expressed in terms of the probability, p, that a given elemental component unit of the lattice, be it an individual site or bond, is active for the process of interest. Hence, for cryoporometry systems, individual pores might correspond to pore bonds in a pore bond network lattice, or regions of pores of similar size might correspond to sites in a site lattice. In cryodiffusometry, the lattice unit will be active for mass transport if it is molten. Therefore, the fraction p will correspond to the fraction of void space that is molten. A critical value of the fraction p is that where a continuous pathway exists that crosses the entire lattice, and it becomes permeable, known as the percolation threshold, p_c. In infinite systems and at infinite times, diffusion vanishes at, and below, the percolation threshold. However, for finite length-scale systems and times, diffusion will still occur. Hence, diffusion can still occur for partially molten cryoporometry systems below the percolation threshold. Below the percolation threshold, over large timescales t, the diffusivity D_s can be described by the scaling law [20,21]:

$$D_s \propto t^{-1} |p - p_c|^{(\beta - 2\nu)}, \tag{5}$$

where β and ν are universal scaling exponents with values of 0.41 and 0.88, respectively, for three-dimensional systems [19]. Hence, (β -2ν) is equal to −1.35. Above the percolation threshold, and for long time-scales, there is an alternative scaling law [20,21] such that:

$$D_s \propto |p - p_c|^{\mu}, \tag{6}$$

where μ is a universal scaling exponent equal to 2 in three-dimensions. In the continuum percolation framework, the number fractions p and p_c are simply replaced in the scaling laws by the volume fractions θ and θ_c [21]. The number fraction p and volume fraction θ can also be equal when number-weighted distributions are derived from normally volume-weighted PSDs assuming that pore length is related to the inverse square of pore diameter [22].

For a three-dimensional system, it is suggested that the connectivity Z of a random pore bond network is related to the percolation threshold by the approximate relation [23]:

$$Zp_c \approx 1.5, \tag{7}$$

2.2. Gas sorption

Capillary condensation in pores is described by the Kelvin equation, which is derived using the Young-Laplace equation, and is written for a cylindrical pore as [24]:

$$ln\left(\frac{p}{p_0}\right) = \frac{\kappa\gamma\overline{V}}{r_c RT} cos\,\varphi, \tag{8}$$

where κ, here, is a geometry parameter and depends on the pore and meniscus type. For a relatively short cylindrical pore open at both ends (through pore), wherein the adsorbed film forms a cylindrical sleeve-shaped meniscus, $\kappa = 1$, while for a pore with one dead end, or for a very long through pore [25], or for desorption, condensation occurs at a hemispherical meniscus such that $\kappa = 2$. γ is the surface tension, $\overline{V}$ is the partial molar volume, R is the universal gas constant, φ is the gas-liquid-solid contact angle (typically assumed to be zero), and r_c is the pore core radius. The characteristic size parameter in the Kelvin equation corresponds to the empty core of the pore, outside the adsorbed film on the pore surface. The actual pore size, r_p, is given by:

$$r_p = r_c + t, \tag{9}$$

where t is the so-called t-layer thickness of the adsorbed multilayer film.

The geometry factor κ in the Kelvin equation provides a simple explanation of the cause of hysteresis in sorption isotherms for capillary condensation in isolated, relatively short, through cylindrical pores open at both ends. In such pores, condensation occurs from a cylindrical-sleeve meniscus along the pore wall, whereas evaporation occurs from a hemi-spherical meniscus at the pore ends. Where this arises, the two different values of the geometry factor κ mean that the relative pressure for the desorption should be the square of the corresponding relative pressures for the adsorption.

From Equation (8), the condensation and evaporation pressures for the same adsorbate in the same pore, or the condensation pressures for the same adsorbate in open/closed pores of the same diameter, can be related via the ratio:

$$ln\left(\frac{P}{P_0}\right)_1 = \frac{k_1 cos\,\varphi_1}{k_2 cos\,\varphi_2} ln\left(\frac{P}{P_0}\right)_2 = \frac{1}{\delta} ln\left(\frac{P}{P_0}\right)_2, \tag{10}$$

where the subscripts 1 and 2 refer to either condensation and evaporation, respectively, or two different pores. For condensation and evaporation, for a relatively short, through cylindrical pore with a fully wetting surface, $k_1 = 1$, and $k_2 = 2$, respectively, and the cosφ_i terms both equal unity. Hence, in that case, the power δ is equal to 2, and the relative pressure for evaporation is the square of the relative pressure for condensation. This case corresponds to the well-known Cohan [26] equations. However, previous work [27], has shown that the power δ to superpose adsorption and desorption branches for non-local density functional theory (NLDFT) kernels calibrated with fumed silica is 1.8. According to Broeckhoff-de Boer theory [28], the equivalent power δ to close single pore hysteresis is 1.5. Studies of templated KIT-6 [29] and disordered silicas [27] have suggested that δ = 1.5 for

three-dimensional, interconnected networks. However, for a fully wetting equilibrium sorption system, with no hysteresis, or very long through pores [25], the power would be unity.

2.3. Comparison of gas sorption with cryoporometry

A unified co-ordinate system, to facilitate comparison between cryoporometry and gas sorption, has been proposed [12,30]. If the meniscus curvature of $2/r$ is considered for both methods, then a general co-ordinate x can be defined as:

$$x = A^{-1}\, ln(z), \tag{11}$$

where A and z are, respectively, $\gamma\, \overline{V}/RT$ and P/P_0 for the Kelvin equation, and $\gamma\, \overline{V}/\, \Delta H$ and T/T_m for cryoporometry.

3. Materials and methods

3.1. Sample

The porous material studied in this work is a commercially available mesoporous, amorphous alumina extrudate, Engelhardt AL3992E, here denoted E2, with diameter ~3 mm. It has a pore volume of 0.595 ml g^{-1} and a (ISO method) BET surface area of 192 m^2g^{-1}. The batch was studied as whole pellets and as a powder sample (with particle size ~100 μm). Previous work has shown that grinding the pellet to powder with a mortar and pestle did not change the mesoporosity [31].

3.2. Nitrogen sorption

The nitrogen adsorption/desorption isotherms were measured at liquid nitrogen temperature (77 K) using a Micromeritics ASAP 2020 physisorption analyser. Adsorption was measured over the relative pressure (P/P_o) range of 0.010–0.995 for adsorption and from 0.995 to 0.100 for desorption. The equilibration interval used was 30 s, with average equilibration times (or average lapsed times) per pressure point being 45 m. The samples were outgassed at 140 °C for 15 h under high vacuum (<1.3 Pa) prior to analysis. Nitrogen desorption scanning curves were performed for the whole and powder samples where the respective ultimate relative pressures on the adsorption boundary curve, where the direction of the pressure change was reversed, were 0.950, 0.900, 0.860, 0.840, and 0.800. Pore size distributions (PSDs) were obtained from nitrogen adsorption isotherms using the Barrett-Joyner-Halenda (BJH) [32] algorithm.

3.3. Mercury porosimetry

Mercury intrusion and retraction curves were measured using a Micromeritics 9520 AutoPore mercury porosimeter over the pressure range of 0.0013–414 MPa covering a pore diameter range of 300 μm to 3.6 nm respectively. The equilibration time used was 15 s, as this had been found long enough to ensure the curves were fully equilibrated.

3.4. Differential scanning calorimetry (DSC) thermoporometry

Experimentation was carried out via a TA Instruments DSC2500 over a temperature range from −50 °C to 5 °C and back to −50 °C, with a scanning rate of 0.5 °C/min. Deionised water was used to soak the sample for 30 min; after soaking, the sample was placed, using a spatula or tweezers, on a wet tissue and then directly in the DSC aluminium pans.

3.5. Magnetic resonance imaging (MRI)

Experimentation was carried out via a Bruker 600 MHz Avance III spectrometer (14.5T), using a 5 mm BBFO SmartProbe. Temperature control was achieved via the Bruker BSVT unit and gas cooling used a Bruker BCU eXtream supplied with dried compressed air. The sample was soaked in deionised water for 30 min. This preparation procedure has been found to lead to complete saturation in previous work [1,18,19]. After soaking, the sample was placed, using a spatula or tweezers, on a wet tissue to remove excess water but retain an exterior film, and then directly in a 5 mmø NMR glass tube with susceptibility plugs both below and above. For powdered samples, water was added with a pipette until a paste-like texture was formed, making sure it was not overly saturated but wet enough. Then, the slurry was placed in a yellow Gilson pipette tip, which was, in turn, placed in the NMR tube. The tubes were sealed using a cap with a wet tissue to ensure the samples did not dry out over time. Cryoporometry experiments were carried out by following a set temperature range after an initial cooling directly from 278 to 235 K to ensure all probe fluid was frozen. Next, the temperature was first raised directly to 250K, followed by a stepwise increase of 0.2 K up to 271 K, using 10 min as equilibration time for each step. Subsequently, the temperature was dropped to 260 K, and then taken back to 278 K using the same step-wise rate as previously. At each temperature step, a spin-spin relaxation time (T_2) filter was applied to selectively detect the signal from the molten phase, and remove that from any remaining frozen phase. The 1D-MRI sequence was a spin-echo sequence with frequency encoding gradient. For the 1D-profile pulse program, the (calibrated) pulse length for the 90° pulse was 11.75 μs, the 180° pulse length was 23.5 μs, the echo time was 428 ms, the delay for gradient recovery was 200 ms, and the eddy current delay was 0.0001 s, and the relaxation delay was 5 s. The peak magnetic field gradient strength used was 2.14 G/cm. The magnetic field gradient used was a smoothed squared pulse (gradient shape SMSQ10) with 10 % attenuation, in order to avoid oscillations at the gradient transitions. The same gradient was used at all temperatures and for the calibration study. The gradient used ensured that the sample was located in the middle of the acquired profile. The resultant resolution of the MRI in the axial direction along the extrudate was 6 μm. Using the calibrated distance-frequency relation described below, the data from the 1-dimensional profile was lumped into 1 mm virtual slices (with ~167 points per slice) to provide a manageable number of slices to make comparisons along the length of the extrudate. Further, lumping the data also allowed the demonstration that the co-operative melting behaviour extended over macroscopic length-scales, since differences were observed over even this size.

It is important to note that the susceptibility plug placed at the bottom of the tube was to ensure that the sample sitting on top of it was directly within the magnetic field, to ensure results are the best representation of structure (which is crucial when spatial 1D-imaging is employed). This region of interest had been initially confirmed using a solution of 10 % D_2O and 90 % deionised water, placed above and below one susceptibility plug. Since physical distances can be measured easily with a ruler, the frequency range of the acquired spectrum could be matched to a distance (equivalent to 730 Hz/mm). Therefore, it could be pointed out where along the NMR tube the signal detection was the highest and where it dissipated, indicating the end of the detection zone. As the presence of the susceptibility plug disrupted the signal acquired, the presence of signal due to the solution followed by its absence, indicated the total frequency region where detection was possible, which was then matched to the physical length of the plug. This confirmed that total length of the region where the frequency signal is the highest and thus is the detection zone where the sample should be placed. This region was calculated to be around 210 mm, placed 10 mm above the bottom of the NMR tube, after its spinner had been adjusted normally with a depth gauge. Thus, the use of a susceptibility plug at the bottom created this buffer, allowing the sample to be within the applied magnetic field.

3.6. NMR cryodiffusometry

Experimentation was carried out via a Bruker 600 MHz Avance III

spectrometer (14.5T), using a 5 mm BBFO SmartProbe. Temperature control was achieved via the Bruker BSVT unit and gas cooling used a Bruker BCU eXtream supplied with dried compressed air. At each temperature tested, a stimulated echo longitudinal eddy current delay (BPLED) pulse sequence with bipolar gradient pulses for diffusion and two spoil gradients, developed by Wu et al. [33], was employed. Initially, two δ values were tested, namely 0.0015s and 0.0022s; 0.0022 was ultimately chosen, as 0.0015 did not show enough attenuation between increasing gradients. The diffusion time, Δ, values chosen ranged from 220 to 300 ms. The pulse separation was 0.0003s. For each diffusion experiment, 9 data points were taken between gradients of 3.41 and 32.35 G/cm, and for each point 232 scans were executed. This ultimately increased experimental times, but the higher number of scans was needed to increase the intensity of the signal acquired and thus make the degree of attenuation much more clear. Diffusion data were also acquired for a fully molten state of the sample at 278K.

4. Results

4.1. Nitrogen sorption

Fig. 2 shows examples of nitrogen sorption boundary adsorption (up to relative pressure of 0.995) and desorption isotherms for whole and fragmented pellets. It can be seen that the adsorption isotherms are smooth curves, very similar to each other. However, both desorption isotherms exhibit two knees, one at a relative pressure of ~0.87–0.91, and one at a relative pressure of ~0.82.

The width of the hysteresis of the gas sorption data, for whole and powder samples of E2, was analysed using the method described in the Theory section, and the results are shown in Fig. 2(c) and (d). For the whole and fragmented samples from batch E2, the values of the power, δ (in eq. (10)) needed to achieve superposition of the adsorption data on the corresponding desorption data at the top of the isotherm were 1.85 and 1.55, respectively, while those needed for the bottom half, below the kink in the boundary desorption, were 1.35 and 1.30, respectively. Hence, as will be seen below, the hysteresis width for E2 is about the same size or lower than that predicted for even the narrowest single pore model. The values of the power δ obtained indicate that the hysteresis width at the top of the loop decreases when the pellet is fragmented, while the width of the lower portion stays roughly the same. The implications of these observations of hysteresis width will be discussed below.

Fig. 2 also shows nitrogen desorption scanning curves for the whole and powder samples where the respective ultimate relative pressures on the adsorption boundary curve, at which the direction of the pressure change was reversed, were 0.950, 0.900, 0.860, 0.840, and 0.800. From Fig. 2, it can be seen that for both whole and powder form samples, the descending scanning curves reach the boundary desorption isotherm before the lower hysteresis closure point. The point of convergence is defined as when the path of the desorption scanning curve becomes parallel with, and therefore tracks the shape of, the boundary desorption isotherm. For example, the scanning curve starting at a relative pressure of 0.9 for the powder sample starts running parallel with the corresponding boundary desorption isotherm at a relative pressure of 0.846. At this point the amount adsorbed on the scanning curve is 97 % of that on the boundary curve. The point of convergence of the desorption scanning curves with each other and the boundary desorption isotherm seems to be at a higher relative pressure for the powder samples compared to the whole pellet samples. This is such that the 0.9 and 0.86 relative pressure desorption scanning curves seem to be more crossing in type, rather than converging, though they do descend some way before reaching other scanning curves or the boundary isotherm [34]. Hence, the curvature of the desorption scanning curve may reflect the large changes in multi-layer thickness (for pores left empty at the top of the scanning curve) in the region of relative pressures that they traverse, as the adsorption isotherm is steep in this range. This can be assessed as follows. Fig. 3 shows the Barret-Joyner-Halenda (BJH) [32] pore size distributions (PSDs) derived, using a hemispherical meniscus in the Kelvin equation each time, from the sorption isotherms for a powdered sample of E2. The BJH PSD algorithm can be used to determine the area of pores that fill above a given relative pressure. If a fractal BET isotherm [5] (see Appendix, Figure A1) is used to predict the multi-layer thinning, as relative pressure dropped from 0.9 to 0.846, in pores that would fill with condensate above a relative pressure of 0.9, and thus would still be empty at the top of the descending scanning curve starting at this relative pressure, then this is found to be 16.2 cc(STP)/g. This estimate of multi-layer thinning compares with a drop of 39.8 cc(STP)/g for the descending scanning curve starting at a relative pressure of 0.9 for the powder sample over the same pressure range. Hence, about 40+ % of the decline in the amount adsorbed, for this scanning curve, as it crosses between the boundary isotherms is associated with multi-layer thinning of unfilled pores. Therefore, the residual drop in the scanning curve, as it traverses the gap between boundary curves, is only ~7 % of the starting amount adsorbed at relative pressure of 0.9. This very small fractional drop, thus, suggests that the scanning curve is predominantly crossing in character. Crossing curves are defined as those scanning curves that decline relatively little in amount adsorbed before they closely approach or reach the boundary desorption isotherm [34].

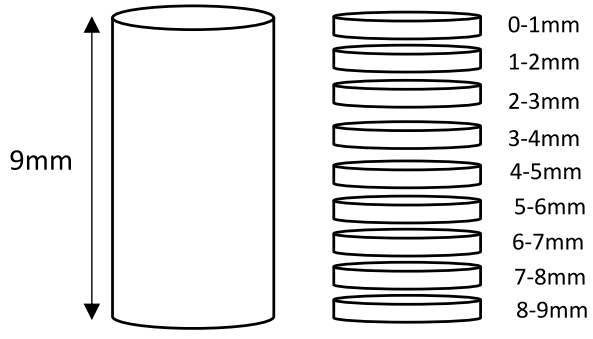

Fig. 1. Schematic diagram of virtual slices for magnetic resonance image of extrudate of E2.

From Fig. 3, it can be seen that the PSDs from the adsorption isotherms are relatively smooth curves, with modal size ~10 nm, whereas the PSD from the desorption isotherm also shows a distinct second modal kink at ~5 nm, corresponding to the second desorption knee. The modal pore size from nitrogen adsorption is similar to that seen in the SEM image given in the Appendix (Figure A2).

The gas sorption isotherms for powder samples of E2 were analysed using percolation analysis generally following the method proposed by Seaton [23]. The BJH PSD was obtained assuming condensation according to a hemispherical meniscus, since simulations suggest long pores approach equilibrium condensation [25]. A power law relationship was assumed between pore diameter and pore length, as done in previous work [22]. The exponent in this power law was obtained by the best fit of the resulting transformed isotherm data to the generalised scaling relationship in the percolation connectivity analysis. For percolation analysis of the boundary desorption isotherm for the powder sample of E2 (used for PSD in Fig. 3), the best fit for the pore length power was −2, and the pore connectivity and lattice size obtained were 2.7 and 6, respectively. Since there is a suggestion of a second percolation transition, in the hump part way down the desorption isotherm, the scanning curve up to an ultimate relative pressure of 0.86 for the powder sample was also analysed using the percolation connectivity analysis. However, this was done using the BJH PSD obtained from the adsorption boundary curve up to the size corresponding (via the Kelvin equation) to the ultimate pressure of the SC. The best fit for the pore length power was −1, and the pore connectivity and lattice size obtained were 2.4 and 3.3, respectively. The connectivity is similar to that obtained for the full boundary curve. The value of pore connectivity of 2.7

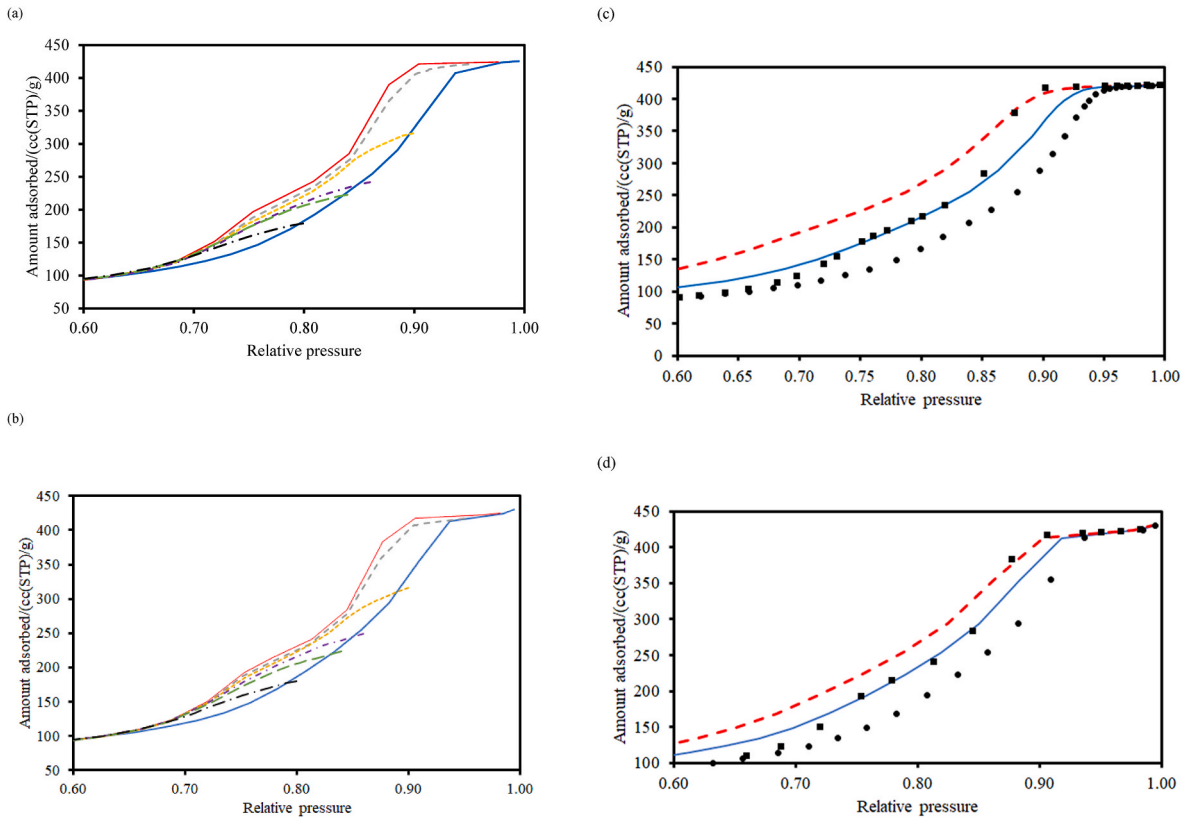

Fig. 2. Boundary nitrogen adsorption (blue thick solid line) and desorption (red thin solid line) isotherms, and desorption scanning curves starting at relative pressures of 0.95 (grey dashed line), 0.90 (yellow dotted line), 0.86 (purple short dash-dot line), 0.84 (green dash line), 0.80 (black long dash-dot line), for whole pellet (a) and powder (b) forms of alumina extrudate E2. (STP = standard temperature and pressure). Analysis of the hysteresis width between boundary adsorption (●) and desorption (■) isotherms for whole (c) and powder (d) samples of E2, with relative pressure points for adsorption raised to high (dashed red line) or low (solid blue line) power δ, as described in the main text.

would mean the percolation threshold for the pore bond network model of E2 would be roughly 0.56, from eq. (7).

4.2. Mercury porosimetry

Fig. 4 shows the mercury porosimetry intrusion and extrusion curves, analysed using the Kloubek [35] correlations calibrated for alumina [31], for whole and powder samples of E2. It can be seen that the Kloubek correlations [31,35] lead to a reasonably close superposition of the extrusion curve on the intrusion curve, thereby suggesting that the contact angle hysteresis has been mostly removed by this processing. It is noted that the mercury intrusion curve in Fig. 4(a) is bimodal with one mode at ~3.5 nm and one at ~5.5 nm. There may be a hint of a third mode at ~8 nm but it is very slight. The mercury extrusion curve for the whole pellet diverges markedly (with a large drop in rate of extrusion) from the intrusion curve at ~6 nm. The level of mercury entrapment is only ~14. %. This suggests there is sufficient shielding of pores larger than ~6 nm to facilitate snap-off of the mercury meniscus and cause the entrapment in the whole pellet. Fragmentation of the pellet leads to a complete loss of entrapment, suggesting the requisite pore shielding has, thereby, been removed.

4.3. Water DSC thermoporometry

Fig. 5 shows the raw melting curve and corresponding cumulative PSD for water DSC thermoporometry obtained using Eq. (1), and a k for melting of water in cylindrical pores of 33.5 K nm, suggested by Gun'ko et al. [6]. From Fig. 5, it can be seen that the melting curve for E2 shows a distinct, long shoulder on the lower temperature side of the main peak. It can also be seen that the resultant cumulative PSD is distinctly bimodal with modes at ~3.5 and ~7 nm, with a Gibbs-Thomson parameter of 33.5 K nm giving rise to a good overlap with the corresponding cumulative PSD from mercury intrusion and the Kloubek [35] correlations, albeit with a difference in shape.

4.4. Water NMR cryoporometry

Cryoporometry experiments were performed for fully water-saturated whole and powder slurry forms of batch E2. The experiments consisted of dropping the temperature to 235 K to ensure the complete pore cores were all frozen. The sample was then warmed stepwise, to obtain the boundary melting curve, until 271 K where the pores were all molten but the external bulk film remained frozen. The temperature was then decreased to obtain the boundary freezing curve. A typical example of a MRI 1D-profile is given in the Appendix (Figure A3). Fig. 6 shows a comparison of the melting and freezing curves obtained for the powder slurry sample by conventional cryoporometry, and individual slices of the whole extrudate obtained by MRI. Fig. 7 shows a pairwise comparison of the melting and freezing curves, obtained via MRI cryoporometry, for each pair of neighbouring, internal slices of a whole extrudate sample. From Fig. 6, it can be seen that the melting curves for the slurry and various slices all coincide for the range of temperatures from the fully frozen sample up to ~268 K, whereupon the curves begin to markedly diverge. The close superposition below 268 K suggests that random errors in temperature and intensity are small, and shows that the later divergences in the curves for individual slices are significant. It can be seen that, past ~268 K, the slurry melting curve is much less steep, and thus melting is delayed to higher temperatures, than for any of the internal slices of the whole pellet sample. From a comparison of the data for each whole pellet slice

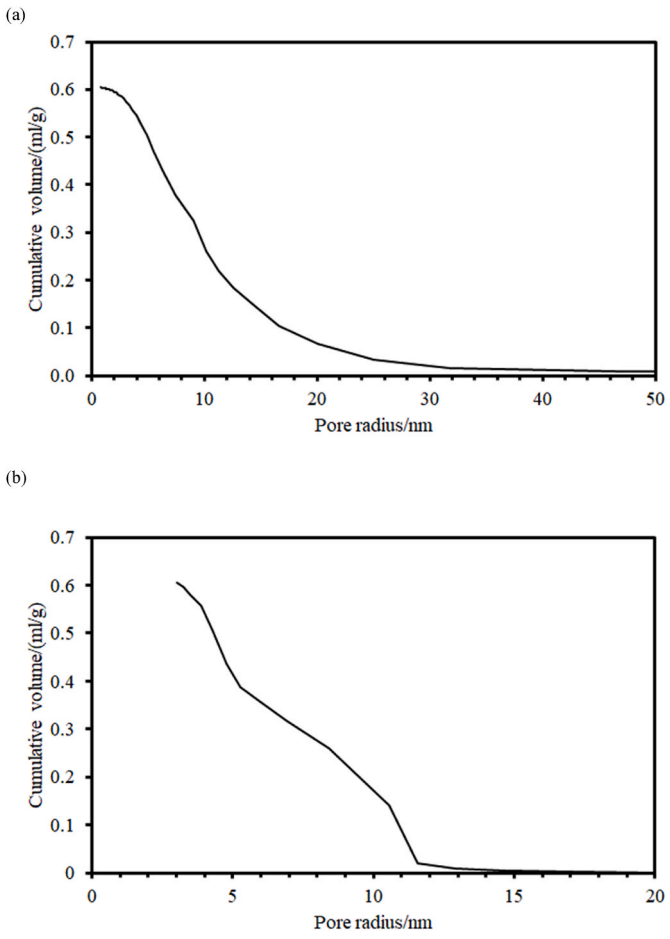

Fig. 3. BJH pore size distributions obtained (with hemispherical meniscus geometry in Kelvin equation) from adsorption (a) and desorption (b) isotherms for powder sample of alumina extrudate E2.

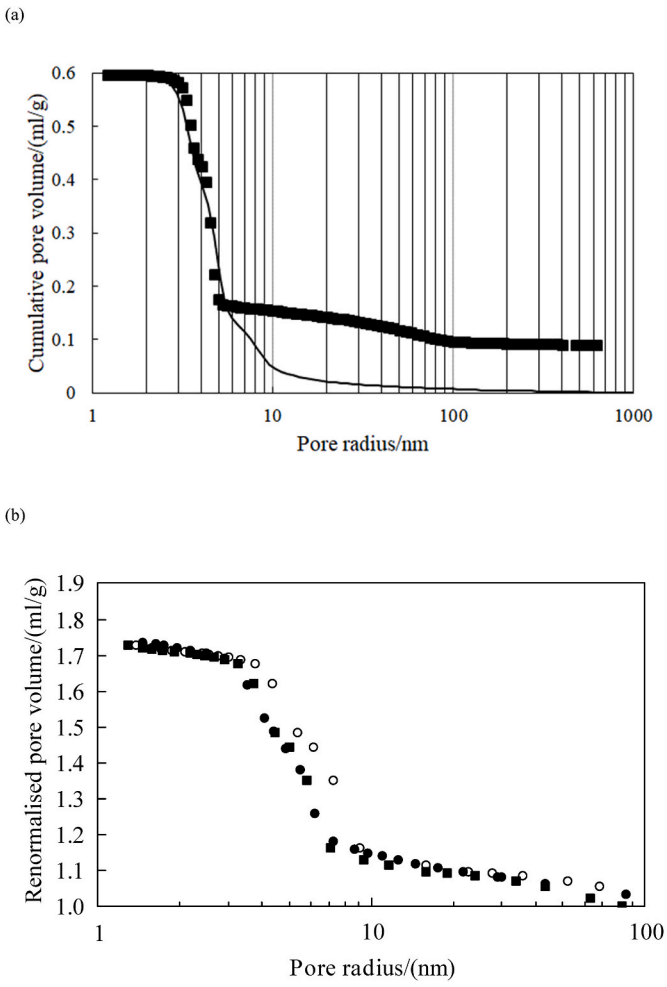

Fig. 4. (a) Mercury porosimetry (solid line) intrusion, and ■, mercury extrusion and amended Kloubek correlation [31], curves for whole pellet sample; and (b) fragmented sample from batch E2. (●, mercury intrusion and original Kloubek [35] correlation; ◯, mercury extrusion and Kloubek correlation; ■, mercury extrusion and amended correlation [31]).

in Figs. 6 and 7, it can be seen that the melting of slices at 3 and 6 mm are delayed to higher temperatures, than their neighbouring slices at 2, 4, 5, 7 and 8 mm. From Fig. 6, it can also be observed that freezing is delayed to lower temperatures for slices 3 and 6 mm, compared to their neighbouring slices at 2, 4, 5, 7 and 8 mm. Overall, it can be seen that while the slopes of the upper parts of the melting and freezing curves for the MR slices are more parallel, the slope of the melting curve for the slurry is much less steep than the freezing curve for the slurry.

From Fig. 6, it can be seen that the upper part (until ~15 % molten fraction) of the freezing curve for the slurry sample occurs at higher temperatures than the corresponding freezing curves for the MRI slices of the whole pellet. The freezing of the whole pellet slices at 3 mm and 6 mm, down to a molten fraction of ~15 %, occurs at a lower temperature than for the other internal slices. The freezing curves for the whole pellet slices crosses the corresponding freezing curve of the slurry sample at a molten fraction of ~15 %, and thus the freezing for the whole pellet slices then occurs at higher temperature than the slurry sample.

The freezing process for the whole pellet sample was halted, at a temperature of 260 K, before the whole pellet pore cores were again completely frozen, where the remaining molten fraction was ~5 %, and the melting re-commenced to construct a melting scanning curve. It can be seen that the melting curves for the slices were all horizontal, and parallel to the boundary melting curve, until a temperature of 264 K was reached. Thereafter the boundary melting curves rose much faster than the scanning curves, until they all converged at a temperature of ~267.5 K (and molten fraction ~8–9 %).

The cryoporometry data for an internal slice (number 6) of the alumina extrudate was compared with that for the gas sorption data for a whole pellet using the unified co-ordinate system described in the Theory section, and the results are shown in Fig. 8. It can be seen that, while the hysteresis width is similar for both data-sets, and the tops of the curves are similar, the gas sorption data covers about twice the range of x for the cryoporometry data. The reason for this difference will be considered in the Discussion below.

4.5. PFG NMR of molten water

The self-diffusivity of water in the molten phase was measured using PFG NMR for a series of molten volume fractions in the range 0.0295–0.4056, corresponding to temperatures in the range 265–270 K, for both the slurry and whole pellet samples. Measurements of the log-attenuation data were obtained at each temperature for separate PFG experiments with differing diffusion times (Δ) of 220, 260, 280 and 300 ms. The log-attenuation plots for the slurry sample data, for these diffusion times at all temperatures, were all very close to straight-lines (coefficients of determination >0.99, as in examples that are given in the Appendix, Figure A4). Therefore, there was no sign of the significant curvature that would suggest restricted diffusion was occurring. Restricted diffusion is when the observed diffusivity depends upon the rms displacement of the molecules (and thus is a function of diffusion time). This is probably because the slurry powder particle size was above one order of magnitude larger than the typical root mean square

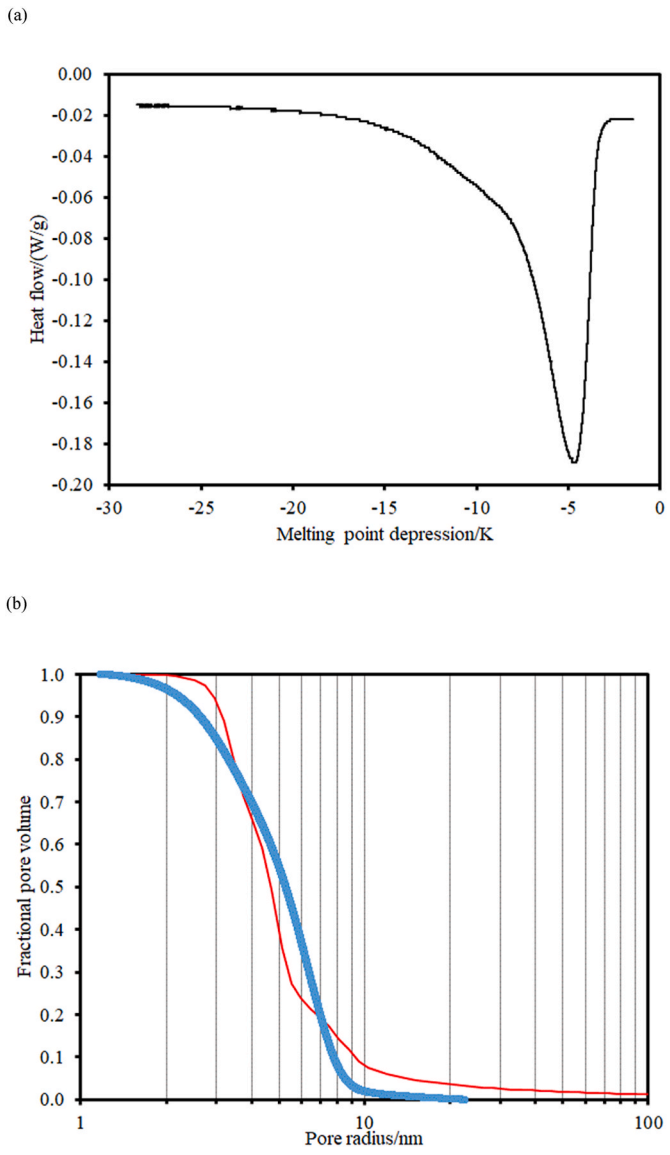

Fig. 5. (a) raw water DSC melting curve, and (b) corresponding cumulative thermoporometry PSD (●) obtained using eq. (1) compared with PSD from mercury intrusion (red solid line), for whole pellet sample of alumina extrudate E2.

displacement (~10 μm) of the molecules during the course of the experiment. Hence, the diffusivities were obtained from straight-line fits to the log-attenuation data. Further, the variation in diffusivities obtained over the aforementioned range of diffusion times (Δ) (~30 % of median time) was not significant compared to experimental fitting error on the log-attenuation plot, so the four diffusivities for each temperature were simply averaged. This average measured diffusivity was converted into a tortuosity value using the corresponding literature value of the bulk diffusivity for the individual temperature. The set of tortuosity values against molten fraction for the slurry sample was then fitted to a power law of the form of eq. (5), assuming the diffusion times are long enough that $t^{-1} \rightarrow \sim$constant for the range studied, with p_c and the scaling exponent as the adjustable parameters. The best fit line to the slurry data is shown as a log-log plot, of eq. (5), in Fig. 9(a). The best-fit values obtained for the percolation threshold and scaling exponent were 0.28 and -1.28 ± 0.26 (where the quoted error is the 95 % confidence interval), respectively.

Fig. 9(b) shows the variation of (unrestricted) tortuosity, for water in the whole pellet sample, with molten volume fraction, starting at values of the latter just below where the melting curves for the whole and slurry samples separated in Fig. 6. From Fig. 9(b), it can be seen that, following the initial decline in tortuosity before the separation of the melting curves for the whole pellet and slurry samples is reached, once it has, then the tortuosity for the whole pellet sample remains virtually constant within experimental fitting error. It is noted that this behaviour contrasts with the variation that would be expected for a completely random arrangement of molten phase, as modelled, say, by a random cluster [5], where the rate of change of tortuosity would be inversely proportional to the square of the molten fraction, rather than independent of it.

5. Discussion

In the following discussion condensation is described as occurring via hemispherical or cylindrical sleeve menisci, according to classical Cohan theory [26]. However, the discussion equally applies to condensation arising in single through pores via the equivalent cases for NLDFT (equilibrium and spinodal kernels). The observed width of the hysteresis for the gas sorption data is narrower than expected from the common theories of single pore hysteresis. This suggests that the pore lengths may be very long. This is because simulations of adsorption in very long pores suggest that the condensation pressure approaches that expected for a hemispherical meniscus, and, thus, there is then no single pore hysteresis [25]. The pores in the samples of E2 might be expected to be considered very long since the pore diameters are ~10 nm but the sample is macroscopic in size (>100 μm). Previous MRI data has also suggested the presence of long-range spatial correlations in local average pore sizes in E2 [17,18]. Therefore, if the pores are very long, then any hysteresis must be pore-blocking in origin. This is consistent with a slight narrowing of the hysteresis at the top of the sorption isotherms on fragmentation of the sample, since the fragmentation process removes some shielding effects. A further consequence of the pores being considered very long, and condensation actually arising due to a hemispherical meniscus, is that there can be no advanced condensation because there is no delay in adsorption in the smallest pores due to condensation then being initiated via cylindrical sleeve menisci. Hence, condensation will occur over a wider range of relative pressures. This is because, if the smallest pores are very long, they will fill at condensation pressures corresponding to a hemispherical meniscus in the Kelvin equation. The capillary condensation region of the adsorption isotherm will then extend towards smaller relative pressures, than for relatively shorter pores.

The gas sorption hysteresis is then dominated by the pore-blocking mechanism. If the disposition of different pores form the equivalent of a simple through ink-bottle pore model, then the shielding smaller pore necks and the shielded larger pore body will each fill at the critical pressures for a hemispherical meniscus in their respective pore sizes. However, desorption from the body will be controlled by the pore neck size, and pore-blocking will result. This would lead to crossing scanning curves at the (larger) relative pressures corresponding to adsorption in the pore body. Indeed, this is what was observed for scanning curves at large relative pressures (e.g. 0.9) for sample E2. The crossing character would decline with relative pressure as less pore-blocking is occurring, and this is what was observed.

While there is no single pore hysteresis for gas sorption, it is still occurring for cryoporometry. The very first melting for E2, for the smallest pores, is still occurring radially from a cylindrical sleeve meniscus. This means that the melting will occur at higher temperatures than it would have done if it had occurred from a hemispherical meniscus. This will shift the bottom part of the melting curve to higher temperatures. This is indeed what can be seen in Fig. 8, the comparison of the cryoporometry data with the corresponding gas sorption data using the unified co-ordinate system. In Fig. 8, the value of the general co-ordinate x at the start of the melting curve is about half that of the corresponding value for the nitrogen adsorption data, as might be

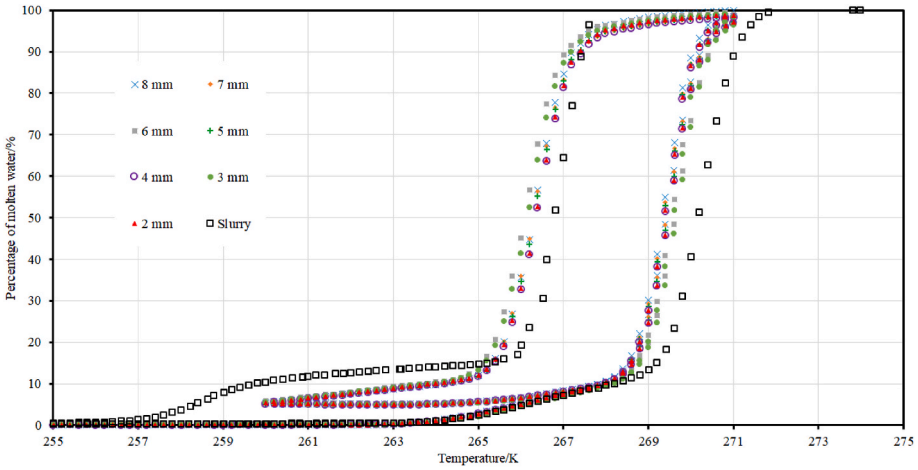

Fig. 6. NMR cryoporometry melting and freezing curves for MRI slices (indicated by distance of nearest edge from one end of extrudate) and powder slurry samples of alumina extrudate E2.

expected if the former is according to a cylindrical sleeve meniscus, while the latter is according to a hemispherical meniscus. Since melting occurs radially in some smaller pores, it can facilitate earlier axial melting in neighbouring larger pores, known as advanced melting. This advanced melting leads to the narrower form of the cryoporometry data compared to the gas sorption data, which lacks equivalent advanced adsorption/condensation effects. The cryoporometry data may be further narrowed, compared to the gas sorption data, if the upper limit to the critical ratio, of the pore body-to-neck size, for advanced melting to occur is larger than the value of 2 predicted by classical theory, as has been suggested in previous work [13].

The similarity in the basic forms of the melting curves for fully saturated, fully frozen whole samples of E2, with a long, more gradual shoulder at lower temperatures, and a larger peak at higher temperatures, suggests that the mode of derivation (DSC vs. NMR) of the melting data does not affect the findings.

It has been seen, in Fig. 6, that the low temperature tails of the freezing curves for the whole pellet slices cross the corresponding freezing curve of the slurry sample at a molten fraction of ~15 %, and thus the freezing for the whole pellet slices then occurs at higher temperature than the slurry sample. This crossing behaviour in the tails of freezing curves was also observed when comparing the experimental freezing curve for nitrobenzene in Vycor porous glass with the expected freezing curve calculated assuming Vycor glass is composed of independent cylindrical pores, and the transitions in them occurred independently at equilibrium with the bulk phase [36]. In overall form, the E2 slurry freezing curve would correspond to the calculated freezing curve for Vycor glass, and the E2 whole pellet freezing curve would correspond to the experimental Vycor freezing curve. The E2 slurry might be expected to behave more like a bundle of independent pores because the fragmentation of the whole pellet removes the previously existing inter-connections between more dispersed parts of the pellet, and stops the progress of cascades due to pore-to-pore co-operative processes, like pore-blocking that occurs in freezing in disordered networks. The freezing occurs at a higher temperature, for the upper part of the slurry curve, than for the corresponding whole pellet MRI slices data, because some of the shielding by narrower pores leading to pore-blocking effects has been removed by the fragmentation of the pellet, as also suggested by the mercury porosimetry data.

It is noted that the percolation threshold value, obtained from the fit of the slurry PFG NMR data to the scaling law (eq (5)), of 0.28 is similar to the theoretical percolation thresholds of 0.29 for randomly overlapping spheres, and 0.29 for a three-dimensional isotropic Poisson polyhedral lattice [37]. It also means that the molten volume fractions for most of the data points in Fig. 9(a) are below the formal percolation threshold. The scaling exponent obtained from the data fit, of 1.28 ± 0.26, is consistent (in that the 95 % confidence intervals overlap) with the value of 1.35 as expected for below the percolation threshold, but the value of 2 expected for above the percolation threshold lies outside the confidence interval. Hence, the fitted values of the percolation threshold and scaling exponent are a self-consistent set, and are those expected for random ordinary percolating systems. Hence, the early stages of melting are a percolation process.

The rapid steepening, with temperature, of the various melting curves in Fig. 6 occurs when there is a consummate rapid expansion in the size of clusters of pores above their critical temperature for axial melting facilitated by molten neighbours. This represents the onset of the growth of percolating clusters of molten pores. The critical phenomenon of this step change is a characteristic of percolating systems. However, the fanning out of the melting curves started a little before the molten fraction reached the formal percolation threshold because the relatively small extrudate and slurry particles are subject to finite size effects, whereby neighbouring lattice units join up to form clusters that are relatively large on the lattice-scale before the overall threshold is actually reached [37]. However, the extrudate MRI slices are larger lattices, meaning more inter-connectivity between regions, than the divided slurry particles, and thus the percolating clusters of molten pores can extend further within the slices and advanced melting can facilitate earlier melting of other pores than for the slurry. This is consistent with the data in Fig. 9(b) showing the approximately constant tortuosity for molten water in the whole pellet sample, once the whole pellet and slurry melting curves separated in Fig. 6, since the water can, typically, then readily explore an extensive, locally, fully molten network in its neighbourhood. When the pellet is broken up into powder some pores are removed from being neighbours of others as the break occurred between them, hence the overall network inter-connectivity between regions is lower for the slurry sample. The melting is thus delayed because, whereas for whole pellets some nucleation sites of early radial melting were once within the same particle as other pores that they then originally helped to melt, after fragmentation they are now separated and the nucleation of melting has to wait for another site still within the powder particle to reach its critical temperature for radial melting. Overall, the powdered sample thus needs more nucleation sites to do the same melting since the co-operative effect of advanced melting has been curtailed by the fragmentation.

The percolation threshold, from the scaling analysis of the PFG NMR data for the cryoporometry melting curve, of 0.28 is different to the value obtained from the analysis of the nitrogen sorption data of 0.55. This difference is in values arises due to the differences in the nature of the respective percolation processes. The advanced melting process is

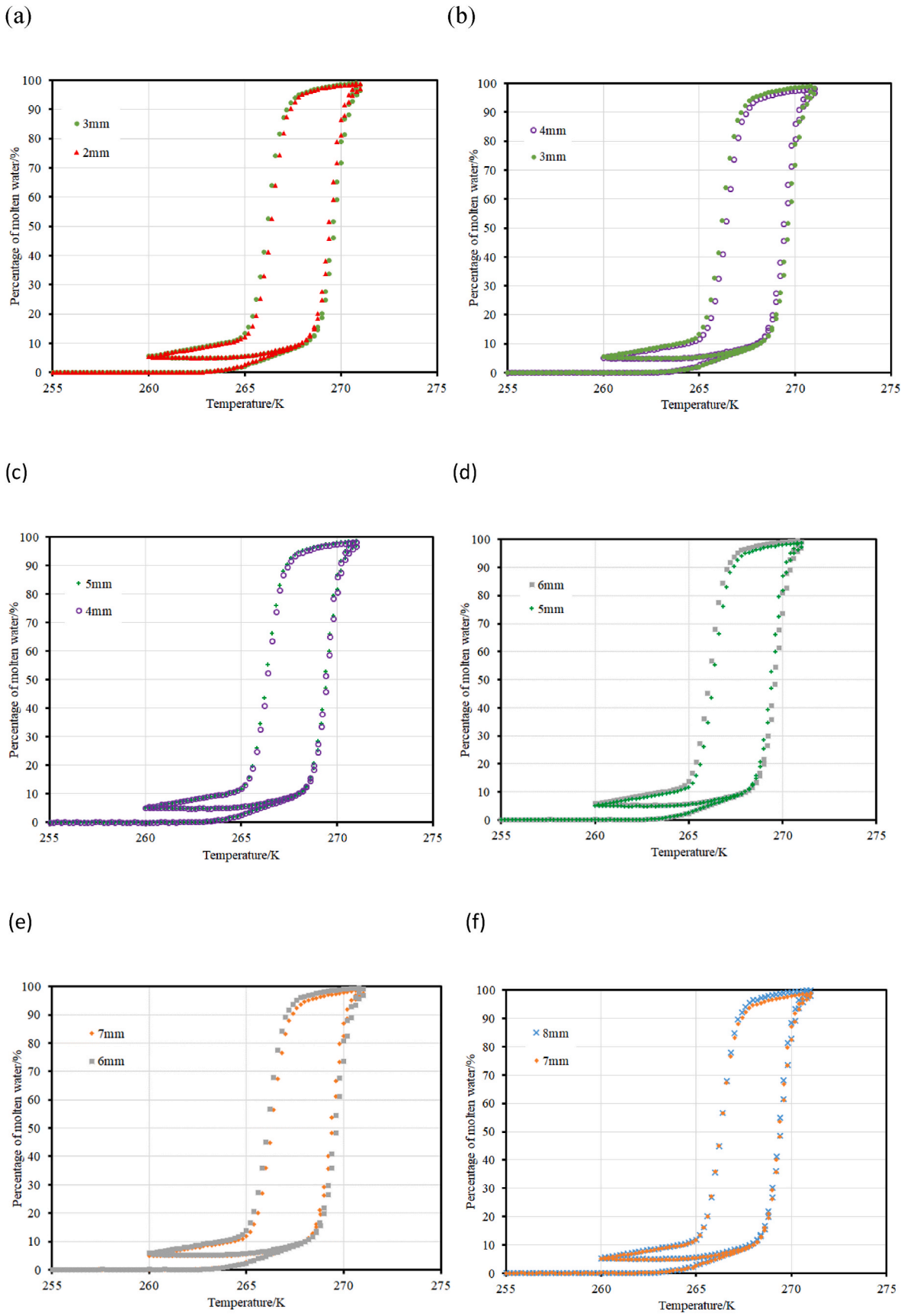

Fig. 7. Pairwise comparisons (a–f) of cryoporometry melting and freezing curves for internal (i.e. non-end) MRI slices of extrudate, each indicated by the distance of the proximal edge from one end of the extrudate, as shown in Fig. 1.

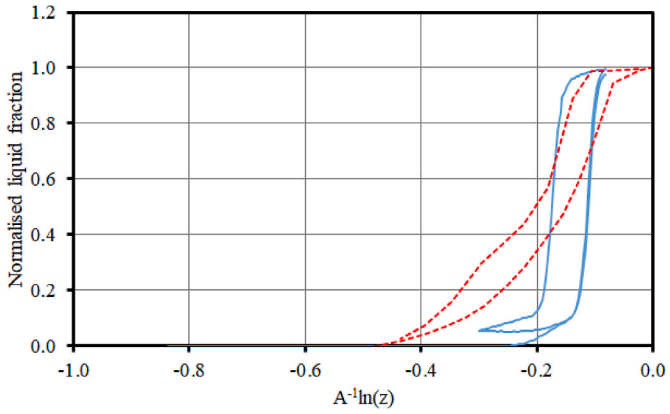

Fig. 8. A comparison of the gas sorption data for whole pellet sample of E2 with the NMR cryoporometry data for slice number 6 (from Fig. 7) using the unified co-ordinate system described in the Theory section. The adsorbate property factor was 0.953 nm, while the Gibbs Thomson parameter used was 52 K nm, working in pore diameter.

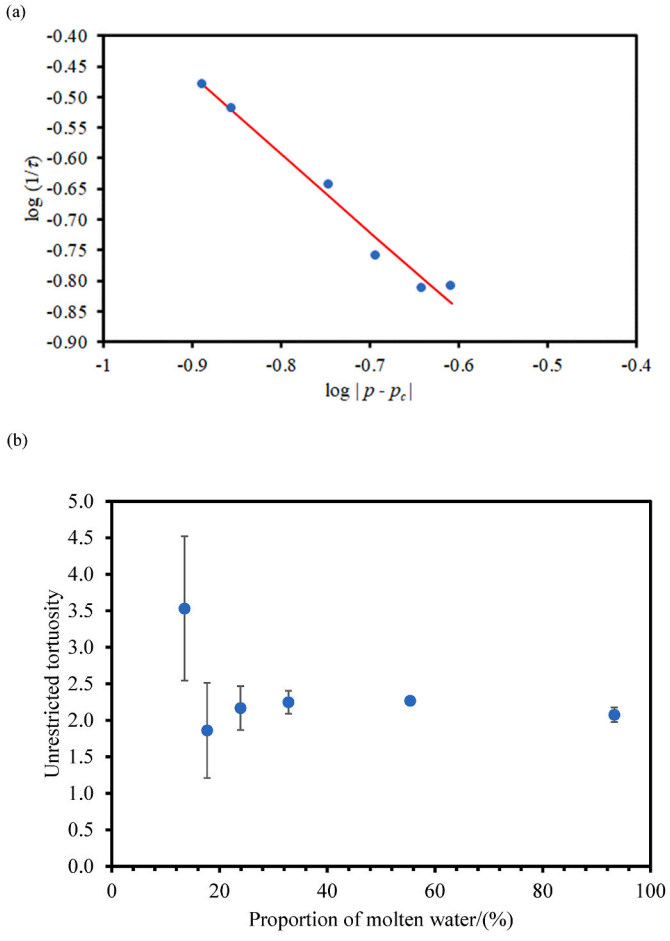

Fig. 9. (a) Log-log plot of scaling law eq. (5) for tortuosityτ ($=D_B/D_{PFG}$) data (●) for the slurry sample derived from diffusivity measured using PFG NMR for various molten fractions p. The solid line is a best-fit straight line to the data points shown. (b) Variation of tortuosity with molten volume fraction for whole pellet sample of E2.

ordinary percolation that can be nucleated pervasively throughout the lattice via radial melting events, while nitrogen desorption is an invasion percolation process initiated by growth inward of (particle) surface clusters of vapour-filled pores. In addition, the model used to fit the nitrogen sorption data was a random bond network, while the Poisson polyhedral structure is a lattice of sites.

The similarity of the percolation threshold found in the scaling analysis to that for a 3D isotropic Poisson polyhedral lattice suggests that the elements of the percolation lattice consist of extended void space regions with similar pore size. This is consistent with the patchwise, macroscopic heterogeneity in the spatial distribution of local average pore size as seen in pore size maps obtained from NMR relaxation time-weighted imaging of individual pellets from batch E2 in previous work [17,38]. Further, the banded variation in the advanced melting and freezing properties along the series of imaged slices of the extrudate, found here, indicated a layering in the structure, which is consistent with the difference in radial and axial directed diffusion observed previously, via MRI, in liquid-liquid exchange experiments on E2 [39]. The progress of the melting and freezing fronts in MR slices starting at 3 and 6 mm may be due to higher pore-blocking and less inter-connectivity within these slices, which would also impact mass transport. Hence, it can be seen how MRI can be used to relate the advanced melting processes in E2 to the pellet macroscopic pore structural heterogeneities, and transport processes within the pellet.

6. Conclusions

Gas sorption scanning curves and mercury porosimetry have shown that the amorphous mesoporous alumina extrudate E2 has heterogeneities but of a limited degree that still means scanning curves can be crossing and mercury entrapment can be eliminated by fragmentation. While it is well known that freezing during cryoporometry is typically an invasion percolation process, due to pore-blocking effects similar to gas desorption or mercury intrusion, the percolative nature of the advanced melting process has been not been much studied until now. The advanced melting process has different idiosyncratic features compared to freezing, including a critical limiting ratio of pore body-neck sizes for the effect to arise, unlike pore-blocking, and a lack of directionality, unlike the invasive in-bound only front during freezing. MRI has been used to study the microscopic spatial distribution of the melting process along the macroscopic length of the extrudate, while PFG NMR was used to measure the connectivity of regions of molten probe fluid at different molten fractions. The initial melting process was found to follow the expected scaling law from percolation theory, and the percolation threshold thereby obtained was that for a 3D isotropic Poisson polyhedral lattice, consistent with the observation of patchwise macroscopic heterogeneities in the spatial distribution of local average pore size in previously-obtained MR relaxation time-weighted images. The MRI has shown that, once advanced melting was initiated, it occurred to different degrees within different slices of the extrudate, such that a banded structure was thereby apparent. This has been seen to be consistent with previous observations of anisotropies in the structure of E2, found by relaxation-time weighted imaging and transient liquid-liquid exchange experiments followed via MRI.

CRediT authorship contribution statement

Eleni Himona: Writing – original draft, Methodology, Investigation, Formal analysis. **Lee Stevens:** Methodology, Investigation. **Huw Williams:** Supervision, Resources, Methodology, Investigation. **Sean P. Rigby:** Writing – review & editing, Writing – original draft, Supervision, Resources, Project administration, Methodology, Funding acquisition, Formal analysis, Data curation, Conceptualization.

Declaration of competing interest

The authors declare that they have no known competing financial interests or personal relationships that could have appeared to influence the work reported in this paper.

Data availability

The data that has been used is confidential.

Acknowledgements

EH and SPR thank the Energy Research Accelerator (ERA) and Innovate UK for the award of a PhD studentship. This work was funded by the Engineering and Physical Sciences Research Council (Grant no. EP/R513283/1).

APPENDIX 1

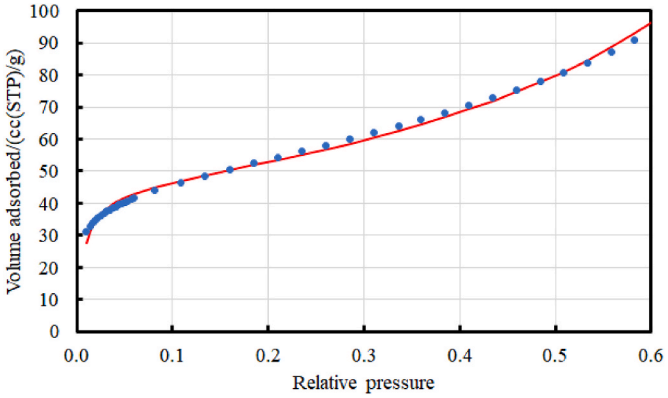

Fig. A1. Nitrogen adsorption isotherm (●) for batch E2 and fit to the fractal BET equation [5] (solid line)

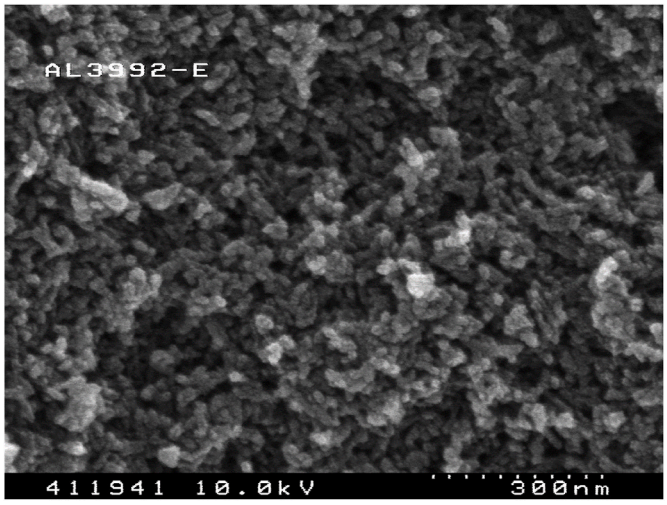

Fig. A2. SEM image of the mesoporosity in alumina E2.

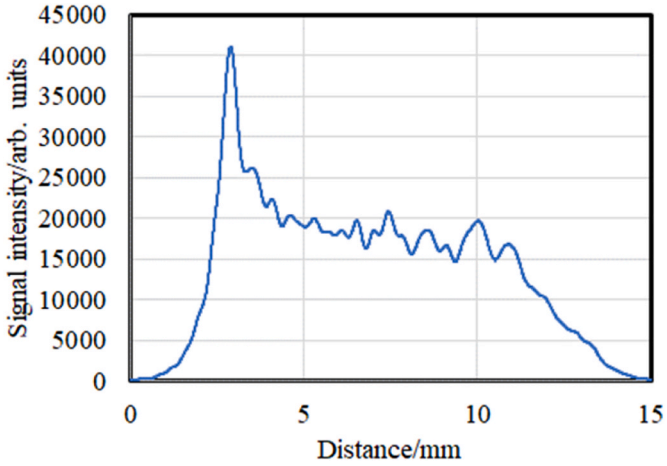

Fig. A3. Example of a 1-dimensional MRI line profile obtained for a sample of E2 during a spatially-resolved NMR cryoporometry experiment at a temperature of 271 K. The resolution is 6 μm. The initial peak at the left hand side corresponds to a bulk film left outside the extrudate.

(a)

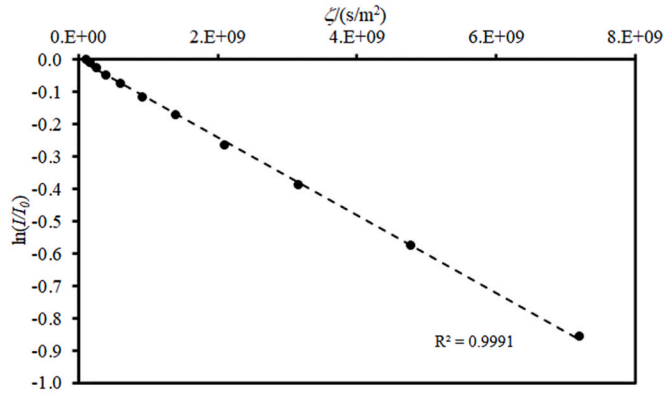

(b)

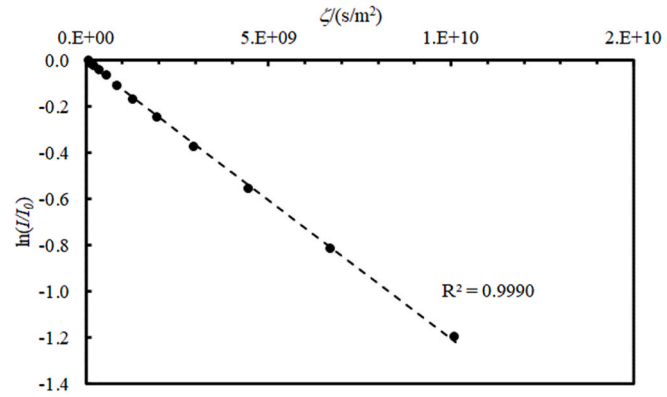

Fig. A4. Examples of PFG NMR log-attenuation plots for fully water saturated slurry sample of alumina extrudate E2, obtained at temperature of 265 K, with diffusion times (Δ) of (a) 300 ms and (b) 280 ms. The parameter $\zeta = \gamma^2\delta^2g^2(\Delta-\delta/3)$, where γ is the gyromagnetic ratio, δ is the gradient duration, and gradient strength *g*.

References

[1] E.L. Perkins, J.P. Lowe, K.J. Edler, N. Tanko, S.P. Rigby, Determination of the percolation properties and pore connectivity for mesoporous solids using NMR cryodiffusometry, Chem. Eng. Sci. 63 (2008) 1929–1940.

[2] N. Gopinathan, B. Yang, J.P. Lowe, K.J. Edler, S.P. Rigby, NMR cryoporometry characterisation studies of the relation between drug release profile and pore structural evolution of polymeric nanoparticles, Int. J. Pharm. 469 (2014) 146–158.

[3] O. Petrov, I. Furó, Curvature-dependent metastability of the solid phase and the freezing-melting hysteresis in pores, Phys. Rev. E 73 (2006) 011608.

[4] V.V. Turov, R. Leboda, Application of H-1 NMR spectroscopy method for determination of characteristics of thin layers of water adsorbed on the surface of dispersed and porous adsorbents, Adv. Colloid Interface Sci. 79 (1999) 173–211, https://doi.org/10.1016/S0001-8686(97)00036-5.

[5] S.P. Rigby, Structural Characterisation of Natural and Industrial Porous Materials: A Manual, Springer International Publishing, Cham., 2020.
[6] V.M. Gun'ko, V.V. Turov, A.V. Turov, V.I. Zarko, V.I. Gerda, V.V. Yanishpolskii, I. S. Berezovska, V.A. Tertykh, Behaviour of pure water and water mixture with benzene or chloroform adsorbed onto ordered mesoporous silicas, Cent. Eur. J. Chem. 5 (2) (2007) 420–454.
[7] A. Schreiber, I. Ketelsen, G.H. Findenegg, Melting and freezing of water in ordered mesoporous silica materials, Phys. Chem. Chem. Phys. 3 (2001) 1185–1195.
[8] T.J. Rottreau, C.M.A. Parlett, A.F. Lee, R. Evans, NMR cryoporometric measurements of porous silica: a method for the determination of melting point depression parameters of probe liquids, Microporous Mesoporous Mater. 264 (2018) 265–271.
[9] S. Mousa, K. Baron, R.S. Fletcher, S.P. Rigby, Triangulation of pore structural characterisation of disordered mesoporous silica using novel hybrid methods involving dual-probe porosimetries, Colloids Surf. A Physicochem. Eng. Asp. 653 (2022) 130026.
[10] I. Hitchcock, E.M. Holt, J.P. Lowe, S.P. Rigby, Studies of freezing-melting hysteresis in cryoporometry scanning loop experiments using NMR diffusometry and relaxometry, Chem. Eng. Sci. 66 (2011) 582–592.
[11] H.R.N.B. Enninful, D. Schneider, D. Enke, R. Valiullin, Impact of geometrical disorder on phase equilibria of fluids and solids confined in mesoporous materials, Langmuir 37 (2021) 3521–3537.
[12] H.R.N.B. Enninful, D. Enke, R. Valiullin, On the comparative analysis of different phase coexistence in mesoporous materials, Materials 15 (2022) 2350.
[13] E. Shiko, K.J. Edler, J.P. Lowe, S.P. Rigby, Probing the impact of advanced melting and advanced adsorption phenomena on the accuracy of pore size distributions from cryoporometry and adsorption using NMR relaxometry and diffusometry, J. Colloid Interface Sci. 385 (2012) 183–192.
[14] M. Wu, K. Fridh, B. Johannesson, M. Geiker, Impact of sample crushing on porosity characterization of hardened cement pastes by low temperature calorimetry: comparison of powder and cylinder samples, Thermochim. Acta 665 (2018) 11–19.
[15] J.H. Strange, J.B.W. Webber, Spatially resolved pore size distributions by NMR, Meas. Sci. Technol. 8 (1997) 555–561.
[16] I. Hitchcock, J.A. Chudek, E.M. Holt, J.P. Lowe, S.P. Rigby, NMR studies of cooperative effects in adsorption, Langmuir 26 (2010) 18061–18070.
[17] M.P. Hollewand, L.F. Gladden, Heterogeneities in structure and diffusion within porous catalyst support pellets observed by NMR imaging, J. Catal. 144 (1993) 254–272.
[18] M.P. Hollewand, L.F. Gladden, Transport heterogeneity in porous pellets-II. NMR imaging studies under transient and steady-state conditions, Chem. Eng. Sci. 50 (1995) 327–344.
[19] D. Stauffer, A. Aharony, Introduction to Percolation Theory, second ed., Taylor & Francis, London, 1994.
[20] S. Havlin, D. Ben-Avraham, H. Sompolinsky, Scaling behaviour of diffusion on percolation clusters, Phys. Rev. 27 (1983) 1730–1733.
[21] A.G. Hunt, B. Ghanbarian, R.P. Ewing, Saturation dependence of solute diffusion in porous media: universal scaling compared with experiments, Vadose Zone J. (2014), https://doi.org/10.2136/vzj2013.12.0204.
[22] S.P. Rigby, M.J. Watt-Smith, R.S. Fletcher, Simultaneous determination of the pore-length distribution and pore connectivity for porous catalyst supports using integrated nitrogen sorption and mercury porosimetry, J. Catal. 227 (2004) 68–76.
[23] N.A. Seaton, Determination of the connectivity of porous solids from nitrogen sorption measurements, Chem. Eng. Sci. 46 (1991) 1895–1909.
[24] S.J. Gregg, K.S.W. Sing, Adsorption, Surface Area and Porosity, Academic Press Inc, London, 1982.
[25] L.D. Gelb, The ins and outs of capillary condensation in cylindrical pores, Mol. Phys. 100 (2002) 2049–2057.
[26] L.H. Cohan, Sorption hysteresis and the vapor pressure of concave surfaces, J. Am. Chem. Soc. 60 (1938) 433–435.
[27] I. Hitchcock, S. Malik, E.M. Holt, S.P. Rigby, Impact of chemical heterogeneity on the accuracy of pore size distributions in disordered solids, J. Phys. Chem. C 118 (2014) 20627–20638.
[28] J.C.P. Broekhoff, J.H. De Boer, Studies on pore systems in catalysis X: calculations of pore distributions from the adsorption branch of nitrogen sorption isotherms in the case of open cylindrical pores, J. Catal. 9 (1967) 15–27.
[29] F. Kleitz, F. François Bérubé, R. Guillet-Nicolas, C.-M. Yang, M. Thommes, Probing adsorption, pore condensation, and hysteresis behavior of pure fluids in three-dimensional cubic mesoporous KIT-6 silica, J. Phys. Chem. C 114 (2010) 9344–9355.
[30] I. Beurroies, R. Denoyel, P. Llewellyn, J. Rouquerol, A comparison between melting-solidification and capillary condensation hysteresis in mesoporous materials: application to the interpretation of thermoporometry data, Thermochim. Acta 421 (2004) 11–18.
[31] S.P. Rigby, New methodologies in mercury porosimetry, in: F. Rodriguez-Reinoso, B. McEnaney, J. Rouquerol (Eds.), Characterization of Porous Solids VI (COPS-VI). Stud Surf Sci Catal, vol. 144, 2000, pp. 185–192.
[32] E.P. Barrett, L.G. Joyner, P.P. Halenda, The determination of pore volume and area distributions in porous substances. I. Computations from nitrogen isotherms, J. Am. Chem. Soc. 73 (1) (1951) 373–380.
[33] D. Wu, A. Chen, Jr.C.S. Johnson, An improved diffusion-ordered spectroscopy experiment incorporating bipolar-gradient pulses, J. Magn. Reson. 115 (1995) 260–264.
[34] G.A. Tompsett, L. Krogh, D.W. Griffin, W.C. Conner, Hysteresis and Scanning Behavior of Mesoporous Molecular Sieves, vol. 21, 2005, pp. 8214–8225.
[35] J. Kloubek, Hysteresis in porosimetry, Powder Technol. 29 (1981) 63–73.
[36] D. Kondrashova, C. Reichenbach, R. Valiullin, Probing pore connectivity in random porous materials by scanning freezing and melting experiments, Langmuir 26 (2010) 6380–6385.
[37] C. Larmier, E. Dumonteil, F. Malvagi, A. Mazzolo, A. Zoia, Finite-size effects and percolation properties of Poisson geometries, Phys. Rev. E 94 (2016) 012130.
[38] S.P. Rigby, L.F. Gladden, NMR and fractal modelling studies of transport in porous media, Chem. Eng. Sci. 51 (1996) 2263–2272.
[39] S.P. Rigby, S. Daut, A statistical model for the heterogeneous structure of porous catalyst pellets, Adv. Colloid Interface Sci. 98 (2002) 87–119.